Imaging condition for elastic RTM

Yuting Duan & Paul Sava
Center for Wave Phenomena, Colorado School of Mines

ABSTRACT
Polarity changes in converted-wave images constructed by elastic reverse-time migration causes destructive interference after stacking over the experiments of a seismic survey. The polarity reversal is due to the fact that S-mode polarization changes as a function of direction, and therefore the imaged reflectivity reverses sign at normal incidence. We derive a simple imaging condition for converted waves imaging designed to correct the image polarity and reveal the conversion strength from one wave mode to another. Our imaging condition exploits pure P- and S-modes obtained by Helmholtz decomposition. Instead of correlating components of the vector S-mode with the P-mode, we exploit the entire S wavefield at once to produce a unique image. We generate PS and SP image using geometrical relationships between the propagation directions for the P and S wavefields, the reflector orientation and the S-mode polarization direction. Compared to alternative methods for correcting PS and SP images polarity reversal, our imaging condition is simple and robust and does not add significantly to the cost of reverse-time migration. Several numerical examples demonstrate the effectiveness of our new imaging condition in simple and complex models.

Key words: elastic wavefields, reverse-time migration, imaging condition

1 INTRODUCTION

Seismic acquisition advances, as well as ongoing improvements in computational capability, have made imaging using multi-component elastic waves, or elastic migration, increasingly feasible. Elastic migration with multi-component seismic data can provide additional subsurface structural information compared to conventional acoustic migration using single-component data. Multi-component seismic data can be used, for example, to estimate fracture distributions as well as elastic and solid-related properties.

In complex geologic environments, it is desirable to use wavefield-based imaging method, e.g. reverse-time migration (RTM). Conventional reverse-time migration consists of two steps: wavefield extrapolation followed by application of an imaging condition (Claerbout, 1971). Wavefield extrapolation requires constructing source and receiver wavefields using an estimated wavelet and the recorded data, respectively. In elastic media, source and receiver wavefields are constructed using elastic (vector) wave equations.

Following wavefield extrapolation, an imaging condition is applied by combining the source and receiver wavefields to obtain images of subsurface structures. Multi-component wavefields allow for a variety of imaging conditions (Yan and Sava, 2008; Denli and Huang, 2008; Artman et al., 2009; Wu et al., 2010). A simple imaging condition for multi-component wavefields is the crosscorrelation of components of the displacement vectors in source and receiver wavefields (Yan and Sava, 2008). In 3D, this results in 9 images for different combinations of source and receiver displacement vector components. One limitation of this method is that P- and S-modes are mixed in the extrapolated wavefields; therefore, cross-talk between P- and S-modes creates artifacts that make interpretation difficult. Another imaging condition for multi-component wavefields first requires the decomposition of wavefields into different wave modes, for example, P- and S-modes. For isotropic elastic wavefields far from the source, P- and S-modes correspond to the compressional and transversal components of the wavefield, respectively (Aki and Richards, 2002). Similar to the imaging condition using displacement vector components, this imaging condition also provides multiple images by cross-correlating different wave modes present in the source and receiver wavefields (Yoon et al., 2004; Yan and Sava, 2008; Denli and Huang, 2008; Yan and Xie, 2012). However, in this case, images correspond to reflectivity for different combinations of incident and reflected P- and S-modes, e.g. PP, PS, SP and SS reflectivity, and therefore are more useful in geological interpretation.

One difficulty when imaging multi-component wavefields is that the PS and SP images change sign at certain incident angles. For example, in isotropic media, polarity reversal occurs at normal incidence (Balch and Erdemir, 1994). This sign change can lead to destructive interference multiple experiments in a seismic survey are stacked for a final image.

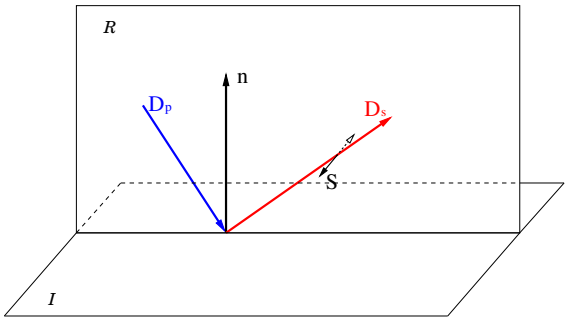
A simple way to correct the polarity reversal in PS and SP images assumes that the polarity change occurs at zero offset and can be corrected based on the acquisition geometry. However, this assumption fails if the reflectors are not horizontal (Du et al., 2012b). An alternative method to correct for the polarity change requires that we compute the incident angles at each image point and then reverse the polarity based on this estimated angle. One possibility is to use ray theory to simulate the incident wavefield direction, and apply this direction to the reflected wave extrapolated from the surface to every imaging point (Balch and Erdemir, 1994). This method is limited by the ray approximation and may become impractical when applied to elastic RTM in media characterized by complex multipathing. Another method to correct for polarity changes is to image in the angle domain, and then reverse the image polarity as a function of angle (Yan and Sava, 2008; Rosales et al., 2008; Yan and Xie, 2012). Constructing angle-domain common image gathers (ADCIGs) is accurate and robust, but can also be expensive. Finally, another possibility for polarity correction is to reverse the polarity in source and receiver wavefields based on the sign of the reflection coefficient, which is computed from the directions of the incident and reflected waves (Sun et al., 2006; Du et al., 2012a). These directions typically are computed using Poynting vectors, which may be inaccurate in complicated models characterized by multipathing (Dickens and Winbow, 2011; Patrikeeva and Sava, 2013).

In this paper, we propose an alternative 3D imaging condition for elastic reverse-time migration. Our new imaging condition exploits geometric relationships between incident and reflected wave directions, the reflector orientation and wavefield polarization directions. Using our new imaging condition, we are able to obtain PS and SP images without polarity reversal. The method is simple and robust and operates on separated wave modes, for example, by the method discussed by Yan and Sava (2008). Our method is also cheap to apply since it does not require complex operations, like angle-decomposition or directional decomposition. We begin by discussing the theory underlying our method and then illustrate it using several simple and complex synthetic examples.

2 THEORY

We propose a new imaging condition meant to compensate automatically for the polarity reversal characterizing conventional images. Our method builds on existing techniques which operate by first decomposing elastic wavefields in pure P- and S-modes. However, in contrasts with more conventional methods, our imaging condition does not simply correlate the P-mode with different components of the vector S-mode. We explain the logic of our method next.

Reconstructed source and receiver elastic wavefields can be separated into P- and S-modes prior to imaging (Dellinger and Etgen, 1990; Yan and Sava, 2008). In isotropic media, this separation can be performed using Helmholtz decomposition (Aki and Richards, 2002), which describes the compressional component P and transverse component $\mathbf{S}$ of the wavefield



(a)

Figure 1. Cartoon describing wave propagation in 3D media. The blue and red lines denote the incident P and the reflected S waves. Vector $\mathbf{n}$ indicate the normal to the interface $\mathcal{I}$, and vectors $\mathbf{D}_p$ and $\mathbf{D}_s$ indicate the propagation directions of the incident P-mode and of the reflected S-mode, respectively. $\mathbf{D}_P$, $\mathbf{D}_S$ and $\mathbf{n}$ are all contained in the reflection plane $\mathcal{R}$.

using the divergence and curl of the displacement vector field $\mathbf{u}$:

$$P(\mathbf{x},t) = \nabla \cdot \mathbf{u}(\mathbf{x},t) , \quad (1)$$

$$\mathbf{S}(\mathbf{x},t) = \nabla \times \mathbf{u}(\mathbf{x},t) . \quad (2)$$

PS and SP images can then be obtained by cross-correlating the P wavefield with each component of the $\mathbf{S}$ wavefield (Yan and Sava, 2008). Images produced in this way have three independent components at every location in space, i.e., PS and SP images are vector images. A side motivation for our method is the fact that it is difficult to find the physical meaning of the various images constructed using this procedure. We seek to avoid vector PS and SP images by combining all components of the S wavefield with the P wavefield into an image representing the energy conversion strength from one wave-mode to another at an interface.

To formulate the imaging condition, we define the following quantities, shown in Figure 1:

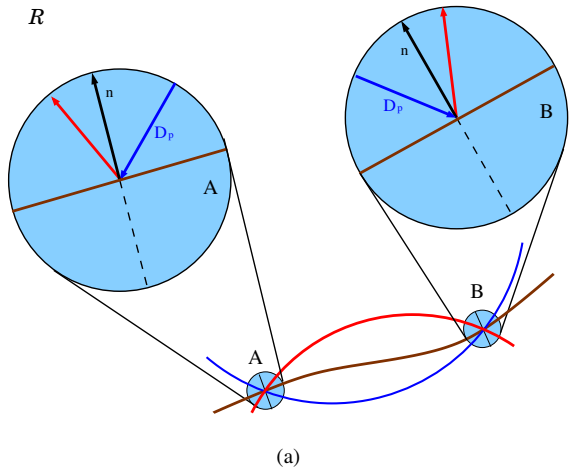
- Vectors $\mathbf{D}_P$ and $\mathbf{D}_S$ indicating the propagation directions of the P- and S-modes, respectively;
- Vector $\mathbf{n}$ which is the local normal to the interface represented by plane $\mathcal{I}$;
- Vector $\mathbf{S}$ which indicates the polarization of the S-mode.

According to Snell's law, vectors $\mathbf{D}_P$, $\mathbf{D}_S$ and $\mathbf{n}$ belong to the reflection plane $\mathcal{R}$. The polarization vector $\mathbf{S}$ is orthogonal to the vector $\mathbf{D}_S$. In the following, we assume that we know the normal vector $\mathbf{n}$, e.g., from a prior image obtained by imaging pure PP reflections.

The polarization vector $\mathbf{S}$ represents waves reflected from incident P or S waves; therefore, the receiver wavefield polarization vector $\mathbf{S}$ is not orthogonal, in general, to the plane $\mathcal{R}$, and can be decomposed into vectors $\mathbf{S}_\perp$ and $\mathbf{S}_\parallel$ such that

$$\mathbf{S} = \mathbf{S}_\perp + \mathbf{S}_\parallel . \quad (3)$$

Vectors $\mathbf{S}_\perp$ and $\mathbf{S}_\parallel$ are orthogonal and parallel to plane $\mathcal{R}$, re-



(a)

Figure 2. Cartoon describing wave propagation in the local reflection plane $\mathcal{R}$. The blue and red lines denote the incident P and the reflected S waves. The wavepaths in the local region around each reflection point can be approximated by straight lines. The black arrow denote the local normal vector to the locally-planar interface.

spectively. The S waves reflected from incident pure P waves are confined to the vector field $\mathbf{S}_{\|}$, so in the analysis of PS reflections, we can simply assume that the S-mode is orthogonal to the reflection plane $\mathcal{R}$. A similar discussion is applicable to SP reflections.

As indicated earlier, the signs of PS and SP reflection coefficients change across normal incidence in every plane, which causes the polarity of the reflected waves to change at normal incidence. Since normal incidence depends on the acquisition geometry, as well as the geologic structure, this polarity reversal can occur at different positions in space, thus making it difficult to stack images for an entire multicomponent survey.

In order to address this challenge, we propose the following imaging condition for PS and SP images:

$$I^{PS}(\mathbf{x}) = \sum_e \sum_t \left(\nabla P(\mathbf{x},t) \times \mathbf{n}(\mathbf{x})\right) \cdot \mathbf{S}(\mathbf{x},t) \ , \quad (4)$$

$$I^{SP}(\mathbf{x}) = \sum_e \sum_t \left(\left(\nabla \times \mathbf{S}(\mathbf{x},t)\right) \cdot \mathbf{n}(\mathbf{x})\right) P(\mathbf{x},t) \ . \quad (5)$$

Here, $P(\mathbf{x},t)$ and $\mathbf{S}(\mathbf{x},t)$ represent the scalar P- and vector S-modes after Helmholtz decomposition, respectively, and $I^{PS}(\mathbf{x})$ and $I^{SP}(\mathbf{x})$ are the PS and SP images, respectively.

The physical interpretation of our new imaging condition, equations 4 and 5, is as follows:

- **PS imaging** (equation 4): The vector ∇P characterizes the propagation direction of the P-mode and can be calculated directly on the separated P wavefield. The cross-product with the normal vector $\mathbf{n}$ constructs a vector orthogonal to the reflection plane $\mathcal{R}$; as indicated earlier, this direction is parallel with the polarization vector of the S-mode, $\mathbf{S}_{\|}$. Therefore, the dot product of $\nabla P \times \mathbf{n}$ and $\mathbf{S}$ is just a projection of the vector S wavefield on a direction which depends on the incidence direction of the P wavefield. For a P-mode incident in opposite direction, the vector $\nabla P \times \mathbf{n}$ is reverses direction, thus compensating for the opposite polarization of the S-mode. Consequently, the PS imaging condition has the same sign regardless of incidence direction, and therefore PS images can be stacked without canceling each-other at various positions in space.
- **SP imaging** (equation 5): The vector $\mathbf{S}$ characterizes the polarization direction of the S-mode, and for the situation considered here it is orthogonal to the reflection plane $\mathcal{R}$. Therefore, vector $\nabla \times \mathbf{S}$ is contained in the reflection plane. The scalar product with the normal vector $\mathbf{n}$ produces a scalar field characterizing the magnitude of the S-mode, but signed according to its relation with respect to the normal $\mathbf{n}$. This scalar quantity can be simply correlated with the scalar reflected P wavefield, thus leading to a scalar image without sign change as a function of the incidence direction. Therefore, SP images produced in this fashion can also be stacked without canceling each other at various positions in space.

In 2D, the imaging condition simplifies. The $\mathbf{S}$ has only one non-zero component, S_y, since the vector $\mathbf{S}$ is orthogonal to the local reflection plane $\mathcal{R}$. Therefore, the PS and SP imaging conditions are:

$$I^{PS} = - \sum_e \sum_t \left(\frac{\partial P}{\partial x} n_z - \frac{\partial P}{\partial z} n_x\right) S_y \ , \quad (6)$$

$$I^{SP} = \sum_e \sum_t \left(\frac{\partial S_y}{\partial x} n_z - \frac{\partial S_y}{\partial z} n_x\right) P \ , \quad (7)$$

where $I = I(x,z)$, $P = P(x,z,t)$, $S_y = S_y(x,z,t)$, $n_z = n_z(x,z)$ and $n_x = n_x(x,z)$. For a horizontal reflector, i.e. $\mathbf{n} = \{0,0,1\}$, we can write:

$$I^{PS} = - \sum_e \sum_t \frac{\partial P}{\partial x} S_y \ , \quad (8)$$

$$I^{SP} = \sum_e \sum_t \frac{\partial S_y}{\partial x} P \ , \quad (9)$$

which simply indicates that in the imaging condition we correlate the P or S wavefields with the x derivative of the S or P wavefields, respectively. That is, of course, just a special case of the more general relation in equations 4 and 5.

We illustrate our new imaging condition with the synthetic model shown in Figure 3(a), which contains one horizontal reflector embedded in constant velocity. Figures 3(b) and 3(c) show the source P-mode and receiver S-mode for the single source indicated in Figure 3(a). As expected, the S-mode changes polarity as a function of the propagation direction. Figure 4(a) is the PS image obtained using the conventional imaging condition, i.e. the cross correlation of the source P wavefield (Figure 3(b)) with the receiver S wavefield (Figure 3(c)), and inherits the polarity change from the S-mode. In contrast, our new imaging condition leads to the image in Figure 4(b) without polarity reversal. This correction allows us to stack multiple elastic images constructed for different seismic experiments.

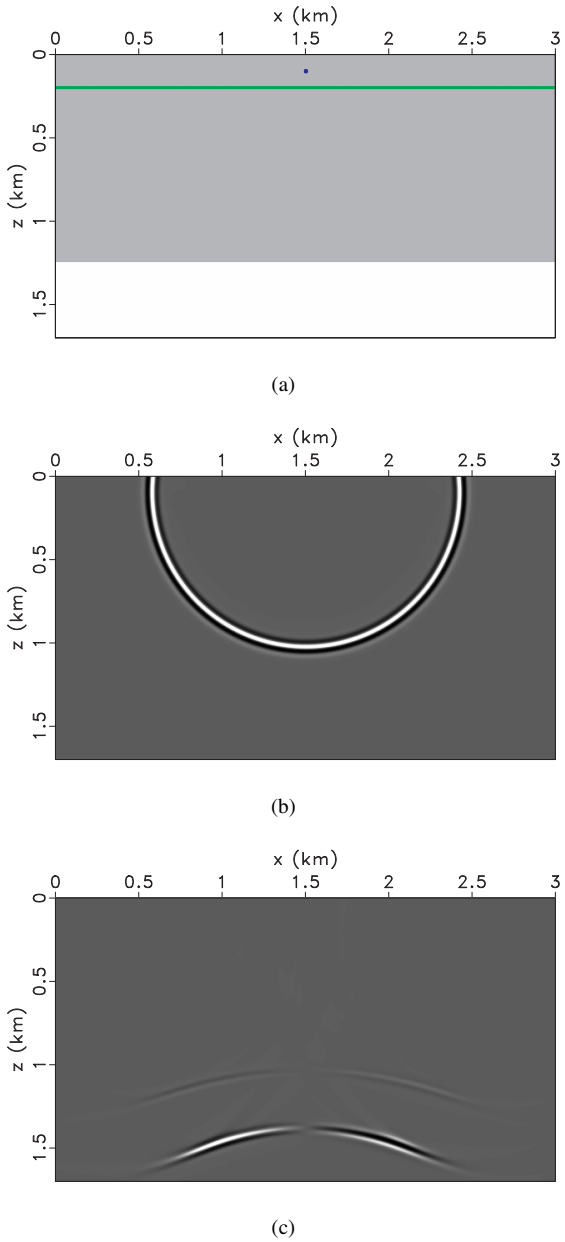


Figure 3. (a) 2D synthetic model with one horizontal reflector in constant velocity. The dot and horizontal line indicate the location of the source and receivers, respectively. Snapshots of (b) the source P wavefield and (c) the S receiver wavefield. The polarity of the source wavefield does not change, in contrast with the polarity of the receiver wavefields which changes as a function of propagation direction.

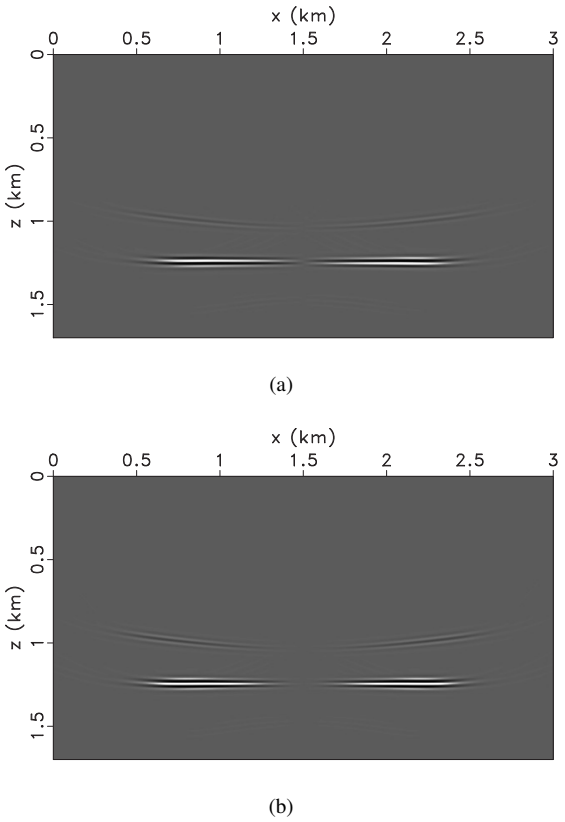


Figure 4. PS images using (a) the conventional cross-correlation imaging condition and (b) our new imaging condition. The image in panel (a) shows polarity reversal, while the image in panel (b) does not.

3 EXAMPLES

We also illustrate our method using two synthetic models.

The first model, Figure 5(a), consists of semi-parallel gently dipping layers. We use 40 sources evenly distributed along the surface, and 500 receivers located at the surface of the model. The source function is represented by a Ricker wavelet with peak frequency of 35 Hz. Figures 5(b) and 5(c) are snapshots of the source P and receiver S wavefields, respectively, and Figures 5(d) and 5(e) are snapshots of the source S and receiver P wavefields, respectively. In both cases, we observe polarity changes in S wavefield.

Using the conventional imaging condition (i.e. cross-correlation of the source and receiver wavefields), we obtain the PS and SP image shown in Figures 6(c) and 9(c). The reflectors on the left side of the model, are not well imaged, due to the fact that the polarity of individual images changes, thus causing destructive interference during summation over shots. The PS and SP common image gathers at $x = 1.5$ km, shown in Figures 7(a) and 8(a), show this polarity reversal causing image destruction.

In contrast, Figures 6(d) and 9(d) show PS and SP images using our new imaging condition. In this case, the interfaces are more continuous compared to the image constructed by the simple cross-correlation imaging condition. Moreover, the PS and SP common image gathers at $x = 1.5$ km, shown in Figures 7(b) and 8(b), confirm that there is no polarity change as a function of shot position.

The second example, Figure 10(a), is a modified Marmousi model. The Marmousi model was created in 1988 by

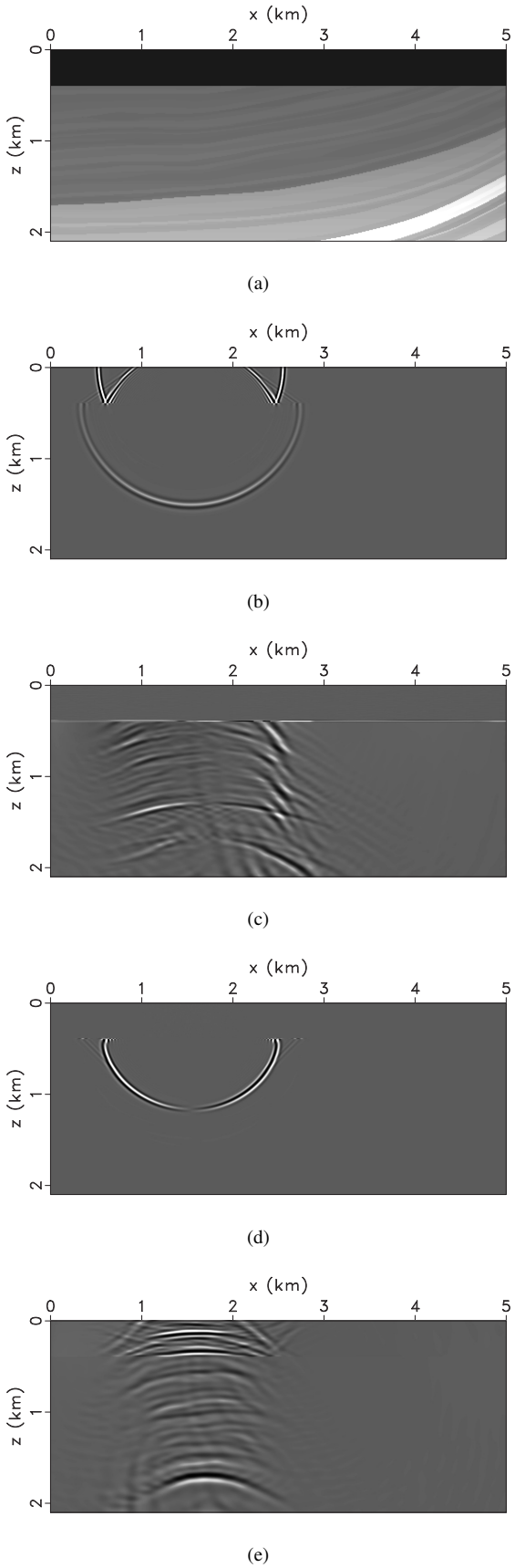


Figure 5. (a) 2D synthetic model with dipping layers; (b) source P wavefield and (c) receiver S wavefield for a single shot; (d) source S wavefield and (e) receiver P wavefield for a single shot.

the Institut Français du Pétrole (IFP). It contains several major faults and semi-parallel dipping layers. We use 60 explosive sources evenly distributed along the surface, and 576 multi-component receivers located at $z = 0.2$ km. The source function is represented by a Ricker wavelet with peak frequency of 35 Hz.

The source S wavefield is weak, due to the minor energy conversion at the top of the model, therefore the SP image is also weak. So in the following, we show only the PS image. Using the conventional and our new imaging conditions, we obtain the PS images shown in Figure 12(c) and 12(d), respectively. The conventional PS image is much weaker than the corresponding image obtained with our new imaging condition. This is due to the fact that the polarity changes as a function of source position occur at different locations in subsurface, and stacking leads to destructive interference between images obtained for different shots. In contrast, our new imaging condition corrects for this effect and leads to images better representing the reflection strength as a function of position in space.

4 CONCLUSIONS

We derive a new 3D imaging condition for PS and SP images constructed by elastic reverse-time migration. As for more conventional methods, P- and S-modes are obtained using Helmholtz decomposition. However, our imaging condition does not correlate various components of the S wavefield with the P wavefields; instead, our method uses geometrical relationships between the wavefields, their propagation direction, the reflector orientation and polarization directions to construct a single image characterizing the PS or SP reflectivity. Our method is simple and robust and leads to accurate images without the need to decompose wavefields into directional components, or to construct costlier images in the angle domain.

5 ACKNOWLEDGMENTS

This work was supported by Consortium Project on Seismic Inverse Methods for Complex Structures. The reproducible numeric examples in this paper use the Madagascar open-source software package (Fomel et al., 2013) freely available from http://www.ahay.org. The authors thank Tariq Alkhalifah for helpful discussions and valuable suggestions.

REFERENCES

Aki, K., and P. Richards, 2002, Quantitative seismology (second edition): University Science Books.

Artman, B., I. Podladtchikov, and A. Goertz, 2009, Elastic time-reverse modeling imaging conditions: SEG Technical Program Expanded Abstracts 2009, 1207–1211.

Balch, A. H., and C. Erdemir, 1994, Sign-change correction for prestack migration of P-S converted wave reflections: Geophysical Prospecting, **42**, 637–663.

Claerbout, J. F., 1971, Toward a unified theory of reflector mapping: Geophysics, **36(3)**, 467–481.

Dellinger, J., and J. Etgen, 1990, Wavefield separation in two-dimensional anisotropic media: Geophysicas, **55(7)**, 914–919.

Denli, H., and L. Huang, 2008, Elastic-wave reverse-time migration with a wavefield-separation imaging condition: SEG Technical Program Expanded Abstracts 2008, 2346–2350.

Dickens, T. A., and G. A. Winbow, 2011, RTM angle gathers using Poynting vectors: SEG Technical Program Expanded Abstracts 2011, 3109–3113.

Du, Q., X. Gong, Y. Zhu, G. Fang, and Q. Zhang, 2012a, PS wave imaging in 3D elastic reverse-time migration: SEG Technical Program Expanded Abstracts 2012, 1–4.

Du, Q., Y. Zhu, and J. Ba, 2012b, Polarity reversal correction for elastic reverse time migration: Geophysics, **77(2)**, S31–S41.

Fomel, S., P. Sava, I. Vlad, Y. Liu, and V. Bashkardin, 2013, Madagascar: open-source software project for multidimensional data analysis and reproducible computational experiments: Journal of Open Research Software, **1**, e8.

Patrikeeva, N., and P. Sava, 2013, Comparison of angle decomposition methods for wave-equation migration: SEG Technical Program Expanded Abstracts 2013, 3773–3778.

Rosales, D. A., S. Fomel, B. L. Biondi, and P. C. Sava, 2008, Wave-equation angle-domain common-image gathers for converted waves: Geophysics, **73(1)**, S17–S26.

Sun, R., G. A. McMechan, C. Lee, J. Chow, and C. Chen, 2006, Prestack scalar reverse-time depth migration of 3D elastic seismic data: Geophysics, **71(5)**, S199–S207.

Wu, R., R. Yan, and X, 2010, Elastic converted-wave path migration for subsalt imaging.: SEG Technical Program Expanded Abstracts 2010, 3176–3180.

Yan, J., and P. Sava, 2008, Isotropic angle-domain elastic reverse-time migration: Geophysics, **73(6)**, S229S239.

Yan, R., and X. Xie, 2012, An angle-domain imaging condition for elastic reverse time migration and its application to angle gather extraction: Geophysics, **77(5)**, S105–S115.

Yoon, K., K. Marfurt, and E. W. Starr, 2004, Challenges in reverse-time migration: SEG Technical Program Expanded Abstracts 2004, 1057–1060.

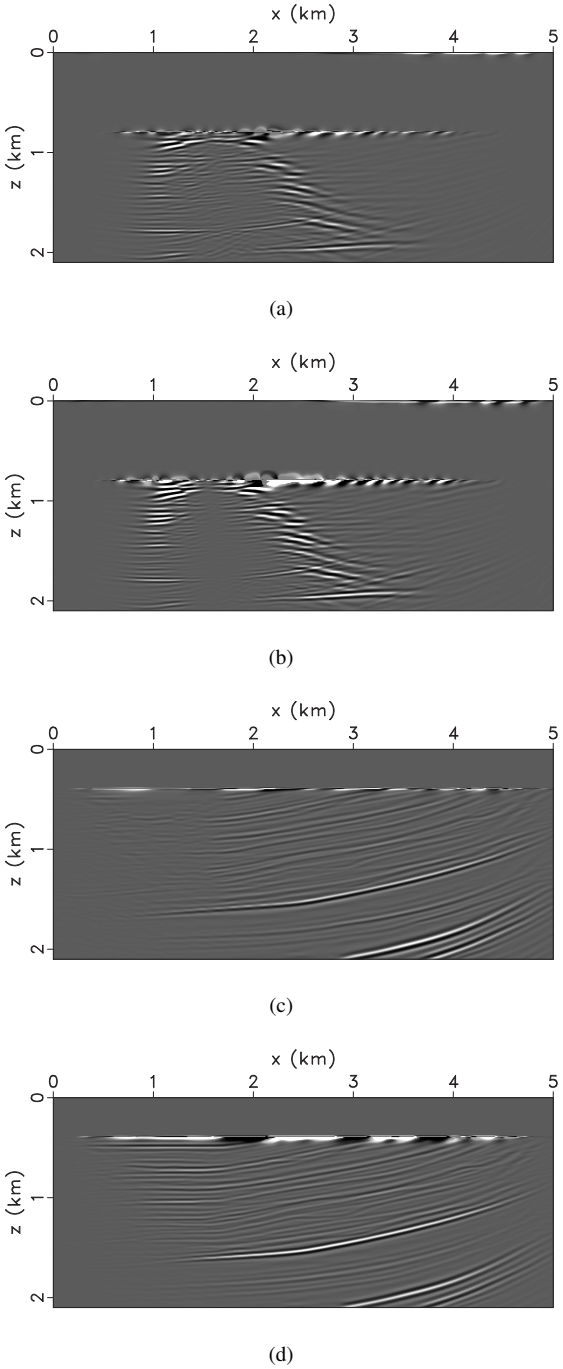
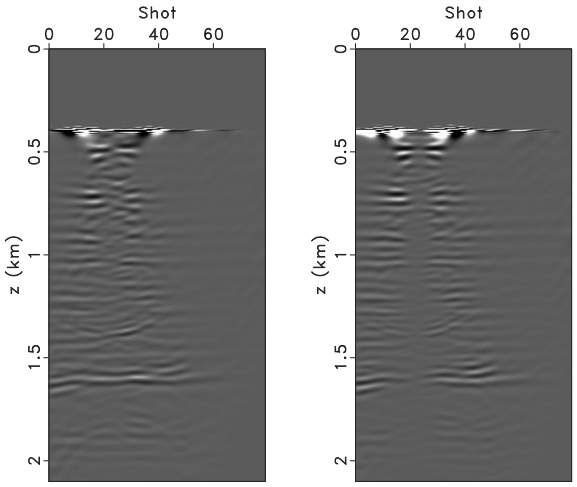
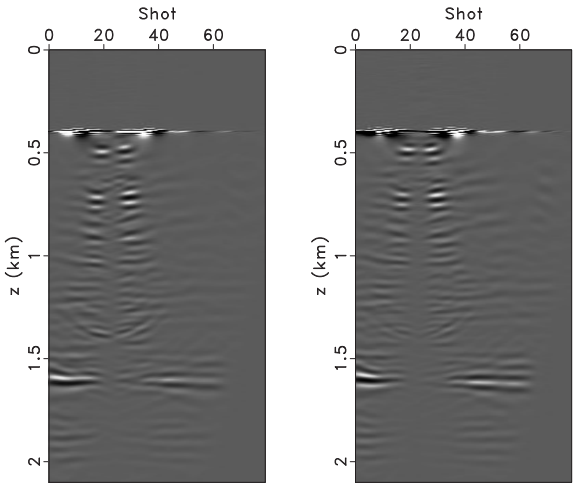


Figure 6. PS images obtained using (a),(c) the conventional imaging condition and (b),(d) our new imaging condition. Panels (a) and (b) depict single-shot images, and panels (c) and (d) depict images obtained after stacking over shot.



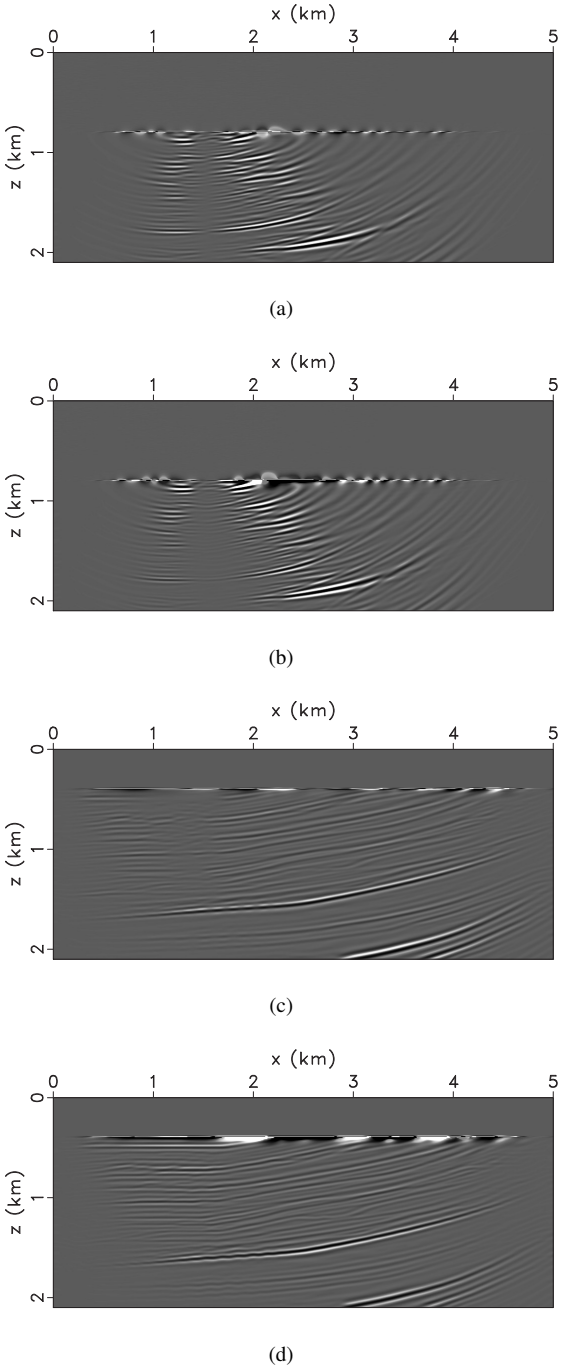
(a) (b)

Figure 7. PS common image gather at $x = 1.5$ km obtained from (a) the conventional imaging condition and (b) our new imaging condition.



(a) (b)

Figure 8. SP common image gather at $x = 1.5$ km obtained from (a) the conventional imaging condition and (b) our new imaging condition.



(a) (b) (c) (d)

Figure 9. SP images obtained using (a), (c) the conventional imaging condition and (b), (d) our new imaging condition. Panels (a) and (b) depict single-shot images, and panels (c) and (d) depict images obtained after stacking over shot.

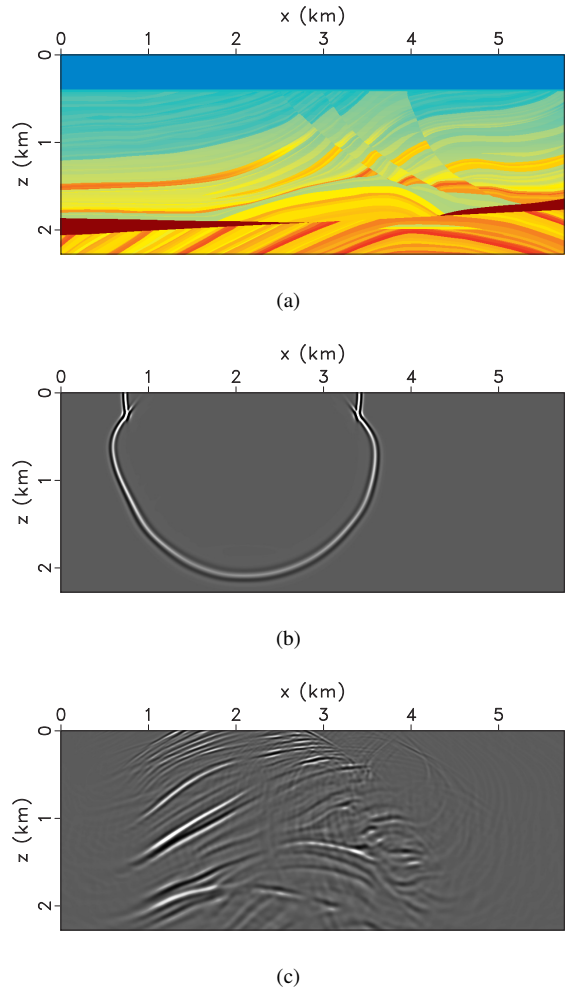


Figure 10. (a) Marmousi model; (b) source P wavefield and (c) receiver S wavefield for a single shot.

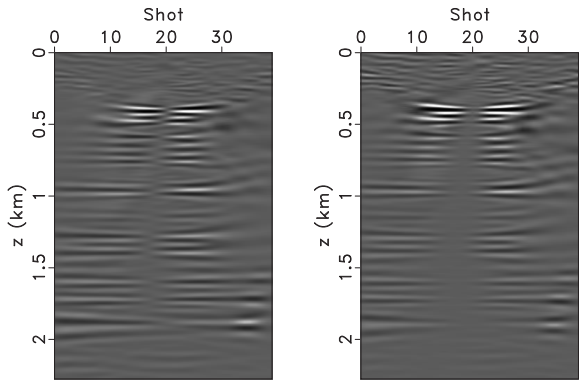


Figure 11. PS common image gather at $x = 2$ km obtained from (a) the conventional imaging condition and (b) our new imaging condition.

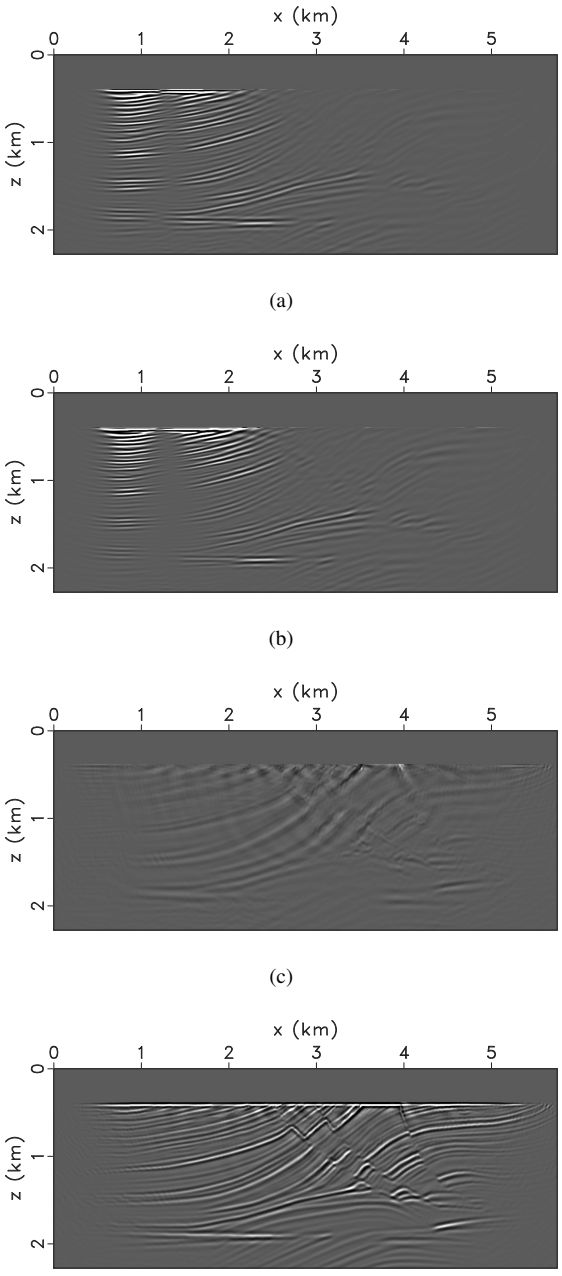


Figure 12. PS single-shot image using (a) the conventional imaging condition and (b) our new imaging condition. PS stack images using (c) the conventional imaging condition and (d) our new imaging condition.